THE JOURNAL OF PHYSICAL CHEMISTRY C

pubs.acs.org/JPCC Article

Enhanced Charge Storage Mechanism and Long-Term Cycling Stability in Diamondized Titania Nanocomposite Supercapacitors Operating in Aqueous Electrolytes

Robert Bogdanowicz,* Anna Dettlaff, Franciszek Skiba, Konrad Trzcinski, Mariusz Szkoda, Michal Sobaszek, Mateusz Ficek, Bartlomiej Dec, Lukasz Macewicz, Konrad Wyrębski, Grzegorz Pasciak, Dongsheng Geng, Arkadiusz Ignaczak, and Jacek Ryl*

Cite This: J. Phys. Chem. C 2020, 124, 15698−15712

Read Online

ACCESS | Metrics & More | Article Recommendations | Supporting Information

ABSTRACT: The long cycle life stability and high energy density are limiting broader feasible applications of supercapacitors (SCs). The novel diamondized titania nanocomposite SCs deliver high power and energy densities along with high capacitance retention rates. SC electrodes were fabricated utilizing a combination of Ti anodization followed by chemical vapor deposition resulting in the simultaneous growth of the complex boron-doped diamond (BDD)/TiC interface. The first-principles simulations along with extended molecular investigations conducted by bright-field transmission electron microscopy and high resolution-scanning electron microscopy revealed that capacitive phenomena are delivered by nanoporous, multifaceted, and substoichiometric TiC, forming clusters at the lateral surfaces of titania nanotubes. Next, TiC mechanical stability and effective charge transfer electrode−electrolyte are efficiently provided by the highly conductive, although discontinuous BDD overlayer. The assembled two-electrode SC devices exhibited capacitances of 15 mF cm^{-2}, which were stable at 0.1 V s^{-1} scan rate in various neutral aqueous electrolytes. The composite TiO_2 nanotube arrays-BDD SCs showed outstanding long-term cycling stability with a capacitance retention of 93% after 100,000 chronopotentiometry cycles verified by postaging cyclic voltammetry tests. In parallel, the energy and power density calculated at a current density of 3 A g^{-1} achieved levels as high as 14.74 W h kg^{-1} and 24.68 kW kg^{-1}, revealing the superior performance of the assembled devices compared to recently reported SCs.

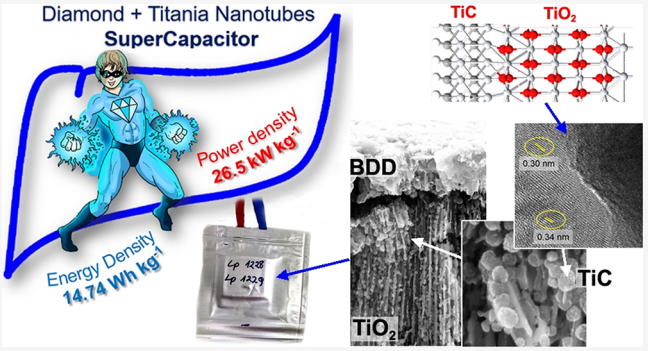

1. INTRODUCTION

The rapid consumption of fossil fuel resources and the severe threat of climate change has caused a shift of attention toward renewable energy sources and efficient energy storage devices. The available lithium-ion batteries have the advantage of a high energy density, but their solid-state reaction limits their power density. On the other hand, the economy of lithium-ion batteries is somewhat limited by various factors, which might be a significant obstacle for large-scale energy storage applications.[1] Supercapacitors (SCs), on the other hand, have an intrinsic advantage of a high power density because the reaction mostly occurs at the electrode surface.[2] Titanium dioxide nanotube arrays (TiO_2NTs) are among the promising materials for SCs. They show a high specific surface area and a direct pathway of charge transport through the nanotubes to the collector (titanium substrate).[3]

To improve the SC performance, several various treatments and modifications have been reported in the literature including doping,[4,5] polymer deposition,[6] forming hybrid capacitors,[7] overgrowth by a porous film,[8] hydrogenation,[9] or nitridation[10] to enhance the electrochemical capacitance of titania nanotubes.

Salari et al.[11] investigated an annealed, highly ordered TiO_2NT array as a SC, reaching a capacitance of up to 0.9 mF cm^{-2}. The low specific capacitances were mainly attributed to poor electrochemical activity and low conductivity, thereby restricting its applications in the construction of high-performance SCs.[12,13] Lu et al.[13] reported that a hydrogenation process led to increased conductivity and electrochemical activity of TiO_2 nanotubes, which could be attributed to the increased donor density and surface-grafted hydroxyl groups

Received: March 29, 2020
Revised: July 1, 2020
Published: July 1, 2020

during hydrogenation. The thermal hydrogenation procedure leads to the increase of capacitance from 0.9 to about 6 mF cm^{-2} after a few cycles[9] and over 7 mF cm^{-2} for titania nanotubes treated with a hydrogen plasma.[14]

Besides the low capacitances of titania nanotubes, the major drawback of presently existing SCs is their limited specific energy.[10] To overcome these issues, various strategies could be undertaken such as the already-mentioned tuning of the capacitor electrode, using an admixture of soluble redox-active species (e.g., $Fe(CN)_6$ 3−/4−)[8] in the working electrolyte or depositing redox-active layers (e.g., metal oxide, conductive polymer or porous carbon films) on the capacitor electrode surfaces.[15−17] The last approach tends to have been playing mainstream role recently because of its radical improvement of electrochemical performance[18] toward SC and super-battery devices.

Various sp^2 rich carbon powders or particles have been widely studied because they require neither current collectors nor organic binders. The sp^3-rich carbon materials open a new prospect for SCs; for example, diamond-coated electrodes enable them to work in aqueous electrolytes, increasing capacitance by their extended working potential range.

For electrochemical capacitors, the amount of stored energy E depends on both the achieved capacitance C and the voltage applied between the electrodes V according to the equation: $E = 1/2CV^2$. Therefore, the operating polarization range is a key factor, although the overall electrochemical performance is of critical importance because the overpotentials can significantly reduce the energy storage capability of a SC.[19] The proper electrolyte provides ionic conductivity and thus facilitates charge compensation on both electrodes of the cell. Recently, the majority of commercial electrochemical capacitors have been based on organic electrolytes with a cell voltage of 2.5−2.8 V. However, their use is associated with a low specific capacitance value, high price, and toxicity. Contrary to this, aqueous electrolytes can offer a higher conductivity, capacitance, and lower environmental impact, but they suffer from narrow electrochemical windows limited by the decomposition of the water. Therefore, the cell voltage is usually limited to about 1 V (although there are new families of aqueous lithium-ion batteries that can perform at high voltages[20]).

Boron-doped diamond (BDD) is widely recognized for its high electrochemical window and chemical stability in aqueous electrolytes, offering not only a high specific capacitance value but also a potentially high energy density and power density and electrochemical stability during the charge−discharge process. The hydrogen-rich plasma used for BDD growth caused vast degradation of titanium collectors, inducing the formation of brittle titanium hydrides. Titania nanotubes (e.g., TiO_2) produced using anodic oxidation on the Ti surface suppress that process because it limits the interactions of the hydrogen plasma with the substrate.

Various porous BDD nanostructures were reported as potential SC electrodes[21] including growth at SiO_2 microspheres as a template on a Ta substrate,[22] electrostatic assembling of nanodiamond seeds,[12] and so forth. Hence, because of the limited scaling of micropores, the porous BDD delivers relatively low capacitance when compared with amorphous carbon or titanium carbide (TiC).[23] However, creating hybrid materials might have a positive impact on the SC performance. TiC, being one of the most promising transition metal carbides with high chemical and thermal stability, and low electrical resistivity[24] is often used as a compound in energy storage hybrid materials.[25] Xu et al.[26] recently reported plasma electrolytic oxidation as an efficient method, also forming a TiO_2 barrier on the titanium substrate. They overgrow such a substrate onto the TiC/BDD composite film, achieving a capacitance of 46.3 mF cm^{-2} along with an energy density of 47.4 W h kg^{-1} and a power density of 2.2 kW kg^{-1}. Nevertheless, the TiC/BDD composite exhibits capacitance retention of 16% after 10,000 cycles mainly because of the degradation of the pores.

This particular work is devoted to the understanding of improved charge storage mechanisms and long-term cycling stability of titania nanocomposites overgrown by BDD for SC purposes. The first-principle simulations along with extended molecular investigations by bright-field-transmission electron microscopy (BF-TEM) and high resolution-scanning electron microscopy (HR-SEM) allows for informative insight revealing the origin of high level and stability of capacitance of TiO_2NT−BDD composites. To our best knowledge, this is the first report revealing complex information about the origin of enhanced charge storage in the TiO_2 nanotube−BDD composite. Next, the series of fully assembled symmetric SCs, utilizing diamondized titania electrodes were also first fabricated and reported. SC investigations include electrochemical properties, capacitances, capacitance retention, and power and energy densities. The use of diamondized electrodes has allowed for an increase of the applied voltage range in aqueous electrolytes.

2. EXPERIMENTAL SECTION

2.1. Preparation of Electrode Layers. Titanium dioxide nanotubes TiO_2NT were obtained via two-step anodization. First, titanium foil (Spinex, grade 1) was chemically polished for 60 s in a mixture of hydrofluoric acid, nitrogen acid, and water with a volume ratio of 1:4:5, respectively. After the chemical polishing process, the titanium foil was degreased in acetone, ethanol, and water in an ultrasonic bath for 10 min each. The anodization process was performed in an electrolyte containing 0.3 wt % of NH_4F dissolved in a solution containing 95% ethylene glycol and 5% water for 60 min under polarization of 60 V at 23 °C. The electrolyte was stirred throughout the anodization process at a speed of 150 rpm. A platinum mesh was used as a counter electrode. After the first anodization was complete, the samples were rinsed with water, dried in warm air, and immersed in a 0.5% solution of oxalic acid for 16 h at 45 °C. Next, the second anodization was conducted under the same conditions. Finally, the samples were immersed in 0.04% hot filament (HF) for 10 s, rinsed with water, and dried. The TiO_2 nanotubes were annealed in a tube furnace at 450 °C for 2 h, with heating steps of 2 °C/min, and left to cool in the furnace. The above procedure was successfully applied in earlier works.[27]

The optimized conditions of the BDD film deposition on a TiO_2NT layer were experimentally investigated, with the deposition carried out using a microwave plasma-assisted chemical vapor deposition (CVD) system (SEKI Technotron AX5400S). The substrates were seeded using a commercial nanodiamond suspension (Blueseeds, AdamasNano, USA) by spin-coating. The induced heated stage was kept at 450 °C and the plasma microwave power was set to 1300 W during the diamond deposition process. The total flow of gas was set to 260 sccm and the CH_4/H_2 molar ratio was kept at 4%. The in-situ boron-doping was held by using diborane (B_2H_6) with the

https://dx.doi.org/10.1021/acs.jpcc.0c02792
J. Phys. Chem. C 2020, 124, 15698−15712

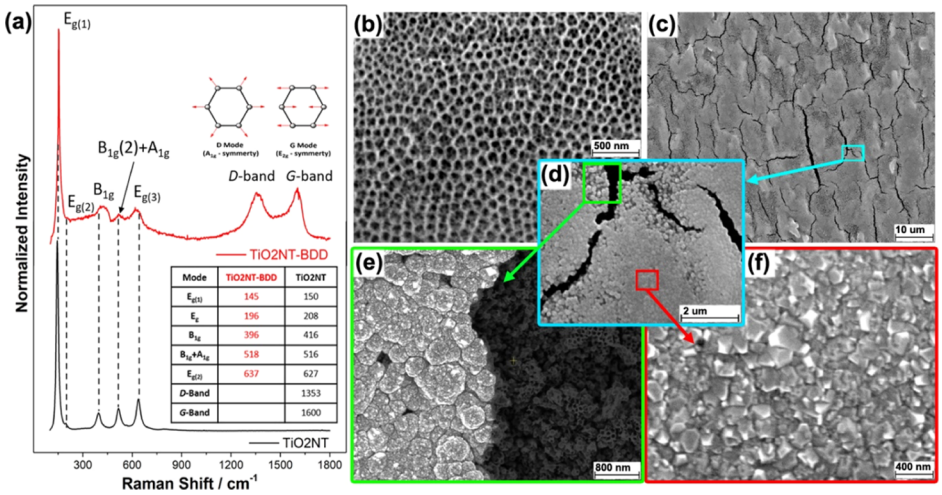

Figure 1. (a) Raman spectra for TiO_2NT and TiO_2NT−BDD, (b) top-view SEM micrographs for TiO_2NT, (c−f) top-view TiO_2NT−BDD images.

B/C ratio at 10,000 ppm. The growth time was 1 h, producing a nanocrystalline film of ca. 300 nm thickness.

2.2. Electrochemical Studies. Electrochemical measurements of the nanocomposite layers were investigated by cyclic voltammetry (CV), electrochemical impedance spectroscopy (EIS) and galvanostatic charge−discharge tests (CP) using a potentiostat−galvanostat (VMP-3, Bio-Logic, France) under the EC-Lab software.

First, the electrode materials were studied in a three-electrode electrochemical cell. The Ag|AgCl|3.0 M KCl, Ag|AgCl electrodes and Pt mesh served as the reference and the counter electrode, respectively. Different types of Ti/TiO_2/BDD were used as working electrodes. For all tested composites, titanium plate served as the substrate. The CV measurements were carried out in contact with 1.0 mol dm^{-3} K_2SO_4, Na_2SO_4, Li_2SO_4, KCl, NaCl, LiCl, KNO_3 aqueous solutions. The charge−discharge measurements were carried out in aqueous electrolytes (1 M $NaNO_3$ and 1 M Na_2SO_4) with a current density equal to 2 mA cm^{-2} (per geometric area of the electrode substrate) in two different polarization ranges: −0.9 to 1.1 and −0.9 to 1.5 V. The EIS was performed in a wide frequency range from 0.05 Hz to 100 kHz in a 1.0 mol dm^{-3} $NaNO_3$ solution. Spectra were recorded at open circuit potential with a peak-to-peak amplitude of 10 mV and 15 points per frequency decade. For all measurements, the electrolytes were initially purged with argon for 45 min in order to remove the oxygen, and all the investigations were carried out in an argon atmosphere.

Electrochemical tests were also performed using fully assembled symmetric two-electrode cells in a coffee bag system. The commercially available foil was used for the preparation of the SC cells. The electrodes were shaped to allow the cells to be prepared without additional electrical contacts wires were connected directly to the uncovered titanium substrate (see the Supporting Information file, Figure S1). The geometric area of one electrode covered by Ti/TiO_2/BDD was equal to 5.76 cm^2. A Whatman paper was used as a separator. An aqueous solution of 1 M KNO_3 was used as an electrolyte.

Coffee bags were enclosed under a vacuum using a Mini Jumbo Henkelman Vacuum System. All of the electrochemical measurements for the SC were performed in a 1 M $NaNO_3$ aqueous electrolyte purged with argon. Analyses were carried out in a two-electrode setup, with both electrodes composed of the reported material. The SC cells were tested using CV (scan rate 200 mV s^{-1}) and multiple galvanostatic charge−discharge cycles (i_k = i_a = 10 mA). The geometric surface area of the tested electrodes was equal to 2.9 cm^2.

2.3. Physico-Chemical Characterization Techniques and First-Principles Approach. SEM JEOL JSM-840 (JEOL, Tokyo, Japan) was used to characterize the topography of the investigated electrodes. The microscope was operating under a 15 kV accelerating voltage. The secondary electron detector working in high vacuum mode (pressure 10^{-4} Pa) was used to observe the structure of the Ti/TiO_2/BDD surfaces. The detailed microstructure and local element distribution of BDD@TiO_2 materials were examined by TEM (JEOL JEM-2200FS) and energy-dispersive system (Oxford Xmax 80T), respectively.

The molecular structure of the pristine and modified TiO_2 nanotube surface was analyzed using the Raman technique. The Raman spectra were recorded using a Raman system (LabRAM Aramis, Horiba Jobin Yvon) at room temperature with a 473 nm diode-pumped solid-state laser for excitation. The spectra were recorded in the range of 100−1800 cm^{-1}.

The X-ray photoelectron spectroscopy (XPS) analysis was carried out using an Axis Supra spectrometer (Kratos Analytical). The spectroscope was equipped with an Al Kα source. The pass energy was 20 eV and the spot size diameter was 2 × 0.7 mm. The instrument was calibrated on metallic gold and copper. The obtained spectra were analyzed using the CasaXPS 2.3.18 software on a Shirley background.

First-principles calculations within density functional theory (DFT) method,[28] available within the program Atomistix ToolKit version 2019.03, QuantumWise Synopsys[29,30] was used for simulation of differential quantum capacitance (QC) of electrodes. The general gradient approximation with Perdew−Burke−Ernzerhof exchange−correlation functionals. Moreover, Fritz Haber Institute (FHI) pseudopotential code was utilized in modeling capacitance properties.

3. RESULTS AND DISCUSSION

3.1. Structure of TiO_2NT−BDD Electrodes. The Raman signals recorded for pristine TiO_2 nanotubes (TiO_2NT) and covered by boron-doped (TiO_2NT−BDD) are shown in

https://dx.doi.org/10.1021/acs.jpcc.0c02792
J. Phys. Chem. C 2020, 124, 15698−15712

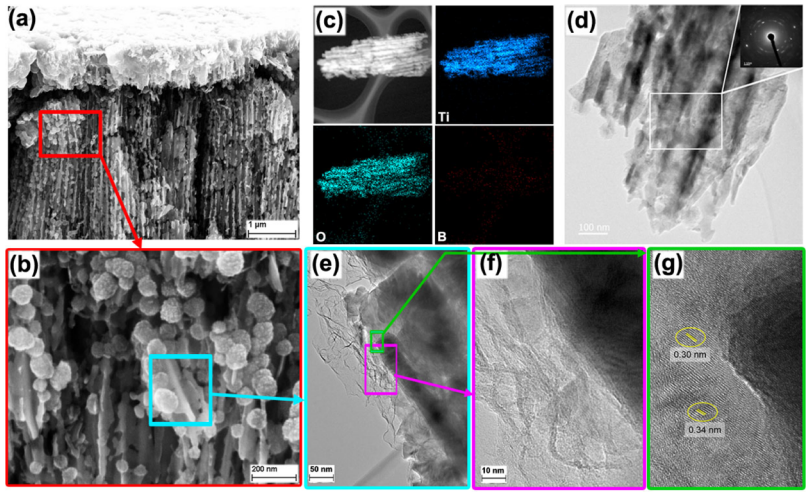

Figure 2. (a) Cross-section SEM image for TiO_2NT−BDD and (b) SEM image emphasized on sp^2-C structures grown on titania nanotubes, (c) element distribution at the nanotube taken from TiO_2NT−BDD sample, (d) low magnification BF-TEM image with the corresponding SAED pattern shown as inset, (e,f) a high magnification BF-TEM micrographs of the TiO_2NT−BDD material corresponding to squared region designated from image (b).

Figure 1a. There are distinguishable bands (145, 396, 518 and 637 cm^{-1}) confirming the dominant allotrope variety of the synthesized nanotubes to be anatase.[31] The TiO_2−BDD reveals Raman bands around 1353 and 1600 cm^{-1}. The first band can be attributed to the disordered carbon (D-band) that is associated with a double-resonance effect,[32] described by a second disorder-induced band at 1350 cm^{-1}. The second band is characterized as the *G*-band correlating to in-plane stretching at 1582 cm^{-1}. The shift of the *G*-band to 1600 cm^{-1} may indicate that graphite present on the outer surface of the nanotube contains sp^2 carbon clusters.[33] Additionally, the carbon associated band shift to 1353 and 1600 cm^{-1} in the TiO_2NT−BDD composite suggests a strong interaction of the BDD with TiO_2 nanotubes, which could enhance the charge transfer between both components, and as a result, hamper charge recombination.[34] Moreover, the Raman spectra reveal that the anatase structure is transformed into a new structure characterized by a Raman band located near 203 cm^{-1}, which is typical for Ti_2O_3.[35] A few slightly shifted bands can also be noticed. Furthermore, noticeable broad signals centered around 416 and 627 cm^{-1} suggest the existence of TiC in the nanotube structure.[36] These signals, together with those around 150 and 516 cm^{-1}, can be attributed to the internal stress of the crystalline structure generated by the TiO_2 and TiC clusters.[37] In their studies on amorphous carbon nanocomposite films doped by titanium, Zemek et al.[38] reported a similar effect, with sp^2 hybridization within subsurface TiC clusters. The appearance of TiC or similar structures during diamond growth in CVD explains the presence of high G and D band intensities on Raman spectra. At the same time, the presence of these two bands may indicate the relatively low quality of the deposited diamond film, as only sp^2-type bonded carbon can be identified. The above-mentioned conclusion is supported by the indefinite shape of the BDD grains at the TiO_2NT−BDD surface.

The surface of the TiO_2NT−BDD electrodes was analyzed using a SEM (Figures 1b−f and 2a,b). The BDD film deposited on the surface of the TiO_2 nanotubes is semi-continuous and covered with micron-sized cracks (refer to Figure 1c). The film consists of nanocrystals ranging in size from 10 to 100 nm, which local differences in the crystallographic structure, in particular in cracks vicinity (Figure 1d−f). The polycrystalline BDD exhibits columnar growth with a highly tailorable microstructure and intergrain porosity. This can be confirmed by previous work.[27,39] The obtained nanotubes have a regular anatase crystalline structure, with the internal diameter and length equal to about 100 nm and 10 μm, respectively. It is noticeable that the morphology of the TiO_2 nanotubes formed in the anodization process is typical for such structures.[40] The reference Raman spectroscopy mapping was performed, revealing the surface homogeneity of the TiO_2NT−BDD electrodes (see the Supporting Information file, Figure S2), which supports the heterogeneous development of BDD crystallites. Furthermore, reported by authors carbon-rich inclusions are well-documented on the HR cross-section SEM image, shown in Figure 2a,b.

Figure 2a shows the cross-section SEM images of the TiO_2NT−BDD electrode, with Figure 2b emphasized on the discussed spherical sp^2 carbon-rich structures, previously reported as TiC clusters. It is clear that the TiO_2NT's are overgrown with these structures and their number is the highest directly beneath the BDD layer. These nanotubes were further analyzed, as shown in Figure 2c−f.

Figure 2c shows the element distribution of TiO_2NT−BDD, indicating that BDD is evenly distributed on the surface of TiO_2 nanotubes. Here the distribution can only be analyzed qualitatively. The selective area electron diffraction (SAED) pattern in Figure 2d reveals high crystallinity and strong electron diffraction. The sheet-like structure of BDD is more clearly revealed by the HR TEM in Figure 2e,f, corresponding to the squared region in Figure 2b. The HR-TEM studies indicate that the TiO_2 core in the size of about 30 nm is encased in much layered carbide-rich phases. Furthermore, the encasing carbide-rich phases have parallel fringes, confirming the well-crystallized nature.

The HF CVD process of BDD growth was previously reported to partially disintegrate the titania nanotubes,[41] when the presence of activated hydrogen and carbon radicals leads to the formation of novel architectures and mixtures of nanophases, including nonstoichiometric titania and titania carbides. Sawczak et al. confirmed these findings through in-depth Raman and XPS studies of TiO_2NT−BDD.[42] Our

https://dx.doi.org/10.1021/acs.jpcc.0c02792
J. Phys. Chem. C 2020, 124, 15698−15712

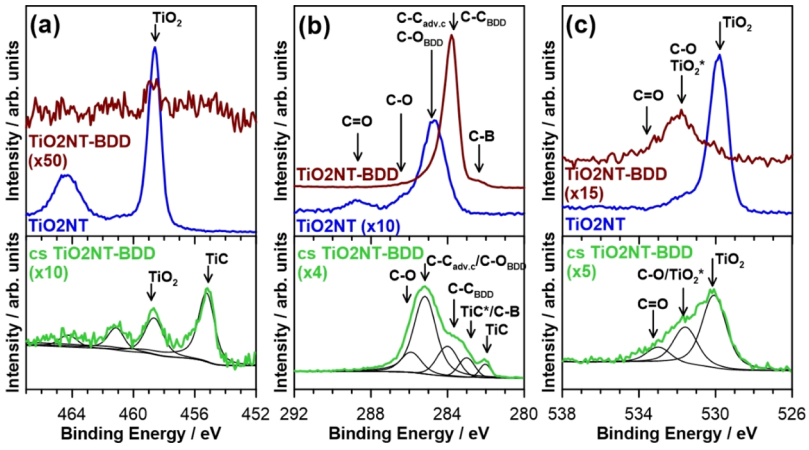

Figure 3. HR XPS spectra recorded for TiO_2NT and TiO_2NT−BDD electrodes in the energy range of (a) Ti 2p, (b) C 1s, and (c) O 1s peaks, and HR-XPS spectra recorded in the cross-section of TiO_2NT−BDD, focused on the carbon-rich structures.

recent findings, based on HR-TEM studies, revealed that the lattices within the carbon-rich growths on titania nanotubes are about 0.3 and 0.34 nm, respectively, which is slightly larger than the DFT calculated Ti−C bond length of 0.224 nm,[43,44] but often found for titanium carbides upon incorporation of oxygen[45] or hydrogen atoms, which is said to increase the lattice parameters.[46] Furthermore, the introduction of vacancies in substoichiometric TiC compounds affects structural relaxations largely increasing the atomic distances.[47]

The HR-TEM images show that the more efficient conducting pathways of ionic diffusion may be played by the pores and cracks present within the BDD layer, as well as the interfacial voids may determine the enhanced capacitive effect of the TiO_2NT−BDD electrodes (refer to Figure 2f). Furthermore, the significant increase in electrode capacitance may be a result of the high development of the electroactive surface area by carbide-rich clusters, which are grown on titania nanowalls. Our HR-TEM images, shown in Figure 2c−e, allow to draw a conclusion regarding low local density, incomparable to this of TiO_2NT and visualized in the form of folding. A similar anomalous increase in carbon capacitance at pore sized less than 1 nm was reported in the literature by the Gogotsi group.[48,49]

Next, the theoretical energetic elaborations of favorable deposition mechanism at the titania nanotubes interface suggest that Ti−C complex requires the lowest bonding energy in that system (435 kJ mol^{-1}).[50] The other potential complexes growing in used microwave plasma composition[51] [OES]: C−C (607 kJ mol^{-1}), C═C (682 kJ mol^{-1}), C−O (1076.5 kJ mol^{-1}), C≡O (1075 kJ mol^{-1})[52] might be synthesized, hence, they are not dominating energetically.

First, it should be raised up that TiO_2NT substrates undergo nanodiamond seeding procedure supporting efficient diamond nucleation, preferring sp^3-rich structure growth. The polycrystalline diamond phase morphology was clearly observed in the SEM. Moreover, Raman mapping extended studies revealed also typical BDD spectra pattern. Certainly, nanodiamond seeds perform here as an effective center of BDD nucleation, where Ti−C phase growth will be limited. Nevertheless, nanodiamond seeds exhibit reduced seeding density at multi-faceted TiO_2NT surface, including weakly-seeded regions inside and at lateral surfaces of nanotubes. These regions would dominantly work as the efficient nucleation sites of Ti−C phase as illustrated in HR-SEM (Figure 2b). Ti−C forms ball-shaped nanoclusters with developed morphology corresponding to the multi-faceted substoichiometric structure. This effect is attributed to the carbide add-layer formation at the tubular nanostructure of anatase TiO_2. In general, the BDD phase undergoes the standard formation mechanism[53] slightly modified by lower seeding density and complex nano-tubular interface. Essentially, conducted CVD process and plasma chemistry during BDD growth induces TiC formation, which was not achievable at other conditions, that is, surface carburization or hydrogenation. Thus, we named this process here as titania nanotube "diamondization" because the BDD does not deliver capacitive effect at the electrode surface.

In details, the proposed molecular growth mechanism Ti−C at the interface of TiO_2NT−BDD composite is following: (I) O abstraction at the growth anatase surface enhanced by presence of atomic hydrogen in plasma, as revealed by An et al.,[54] (II) reactive H radicals lead to breaking of the weaker bonds, creating dangling titanium bonding, (III) attachment of a CH_x radicals to the titanium surface due to the lowest Ti−C bond energy of 435 kJ mol^{-1}, which are responsible for the enhanced electrochemical performance and developed morphology; (IV) bridging of these adsorbates induced by (V) constant H abstraction in hydrogen rich plasma. The devised mechanism is directly corroborated with shown below TEM imaging, XPS and Raman data, revealing significant content of TiC phase. It delivers large capacitances in bulk,[55] nanoporous,[56] or 2D forms.[23,57]

Figure 3 shows the HR XPS spectra recorded for the studied TiO_2NT and TiO_2NT−BDD electrodes in the energy range of Ti 2p, C 1s and O 1s peaks. The spectra obtained for TiO_2NT in Ti 2p energy range (Figure 3a) reveal a single chemical state with a Ti $2p_{3/2}$ peak located at 458.7 eV characteristic of TiO_2 in the form of anatase.[40,58−60] Upon BDD deposition, the share of titanium on the electrode surface is vastly diminished, yet still somewhat noticeable, which is mostly due to reported discontinuity and localized growth of the BDD film. Importantly, the peak position of titanium oxide remnants on the electrode surface is not altered.

The C 1s and O 1s peaks (Figure 3b,c, respectively) prove the successful deposition of a BDD thin film on top of the TiO_2NT surface. The principal constituent of the TiO_2NT−BDD surface is carbon (95.2 at.%), with its primary component located at approx. 284.0 eV, a value frequently

https://dx.doi.org/10.1021/acs.jpcc.0c02792
J. Phys. Chem. C 2020, 124, 15698−15712

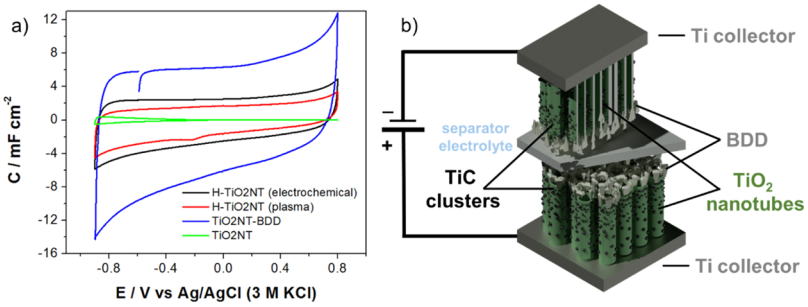

Figure 4. Comparison of CV curves recorded for unmodified TiO_2NT, TiO_2NT−BDD, electrochemically hydrogenated TiO_2NT, and hydrogen plasma-treated TiO_2NT (a) along with scheme of the electrode system and components.

reported and characteristic of a hydrogenated BDD surface. The share of C−C_{BDD} component exceeds 90% of the total carbon contribution. The second component of the deconvoluted TiO_2NT−BDD C 1s peak is positively shifted by +1.3 eV versus the primary component and attributed to adventitious carbon, typical for air contamination and oxygenated termination bonds on the BDD electrode surface.[61,62] Finally, a small contribution is observed at approx. 283.0 eV, characteristic of carbon−boron interaction within BDD. On the other hand, the C 1s chemistry of the bare TiO_2NT electrodes suggests some presence of adventitious carbon contamination and residues of the organic compounds used during the anodization process, its share not exceeding 14 at. %. The chemistry of the O 1s peak for the TiO_2NT electrode surface corroborates the TiO_2 presence, with a peak at 529.9 eV. Furthermore, the O 1s-TiO_2 to Ti $2p_{3/2}$-TiO_2 ratio is 2.12:1. Two smaller O 1s features, shifted toward a more positive binding energy (BE) values should be attributed to C−O and C═O, which result from glycol residues within the NTs, and storage of the electrodes in atmospheric air. The surface hydroxyl species and nonlattice oxygen within the TiO_2 structure will overlap the component peaking at 531.7 eV.[63] For the TiO_2NT−BDD electrode, the only source of oxygen originates from the adsorption of contaminants from the air atmosphere.

The HR XPS spectra were also recorded in the cross-section of the TiO_2NT−BDD layer, analogous to one shown in Figure 2b, with the goal to provide a chemical description of carbon-rich nanostructures grown on the titania nanotubes. Here, apart from the signal originating from TiO_2, a strong Ti $2p_{3/2}$ peak indicating titanium−carbon interaction is clearly visible at 455.0 eV.[42,64,65] The presence of titanium carbides is further confirmed based on the shape of the recorded C 1s spectrum, where two components appear, which are characteristic for TiC. The TiC component (BE at 282.1 eV) and TiC* (283.0 eV) were previously reported for amorphous carbon films containing nanocrystalline titanium carbides.[64,66] Lewin et al. conclude that the share of TiC* in the recorded spectra increases significantly with smaller grain sizes. Here, the major C 1s component (BE at 285.1 eV) originates primarily from amorphous carbon and carbon−oxygen interaction in BDD-like structures. The above-presented model is further supported by the O 1s spectra deconvolution.

3.2. Electrochemical Characterization of TiO_2NT−BDD Composite Electrodes. Electrochemical studies of the TiO_2NT−BDD nanocomposite electrodes were carried out in order to evaluate their utility as an electrode material for SC. Electrodes were tested in three-electrode electrochemical cell and two-electrode symmetric supercapacitor as shown in Figure 4b. The CV curves recorded for the differently pretreated TiO_2NT electrodes are shown in Figure 4a. The measurements were carried out in the potential range of −0.9 to +0.8 V versus AglAgCl|3 M KCl with a scan rate equal to 100 mV s^{-1}.

All modified electrodes display a highly rectangular shape without redox peaks, which indicates a capacitive nature of the electrodes. CV results show good charge−discharge reversibility of the composites. Another one of the reported reasons for the capacitance enhancement of the TiO_2NT−BDD composite may be related to the hydrogenation phenomenon that occurs in the deposition chamber during BDD sputtering.[13,67] However, it is clear that the enhancement of the capacitance induced by the BDD layer deposition at the TiO_2NT surpasses the one offered solely by hydrogenation of the TiO_2NT surface, in studied aqueous electrolyte. The CV curves recorded for unmodified TiO_2NT, shown for comparison, exhibits negligible capacitance.

Even though the electrochemical route of hydrogenation gives better results than hydrogen plasma treatment, the obtained results do not vary significantly. On the other hand, the hydrogen plasma treatment was performed under the same parameters as the BDD deposition, but without a source of carbon and boron, proving the positive impact of diamondization on energy storage ability. Interestingly, BDD deposited, for example, on silicon wafers, does not show the ability to store an electric charge,[68] which compose a valuable rationale for the hypothesis regarding capacitance increase by carbide-rich structures overgrowing the titania NTs. Recently, the enhanced capacitive effect was attributed to the transformation of TiO_2 to Ti_2O_3 and nonstoichiometric TiC,[53] while our BF-TEM studies showed that it is delivered by nano-cylindrical and multi-faceted TiC clusters nucleated by surfaces defect at the inter-tubular interfaces of TiO_2NT array.

The TiO_2NT−BDD electrode was then investigated in different neutral aqueous electrolytes at a concentration of 1.0 mol dm^{-3}: K_2SO_4, Na_2SO_4, Li_2SO_4, KCl, NaCl, LiCl, and KNO_3. We decided to use neutral pH because in such an environment it is possible to utilize wider operating polarization range, which offers a stable response from the studied material, compared to acidic and basic electrolytes.[69] As seen in Figure 5, the TiO_2NT−BDD composite layers display the same highly rectangular shape without redox peaks and good charge−discharge reversibility. Moreover, the type of electrolyte ion, both anion, and cation, only slightly affects the current density of the electrode layer in the investigated polarization range (−0.9 to 0.8 V vs AglAgCl|3 M KCl). Because of the various hydrated ion sizes and the various ionic conductivities of studied ions, we expected different capacitances of the

https://dx.doi.org/10.1021/acs.jpcc.0c02792
J. Phys. Chem. C 2020, 124, 15698−15712

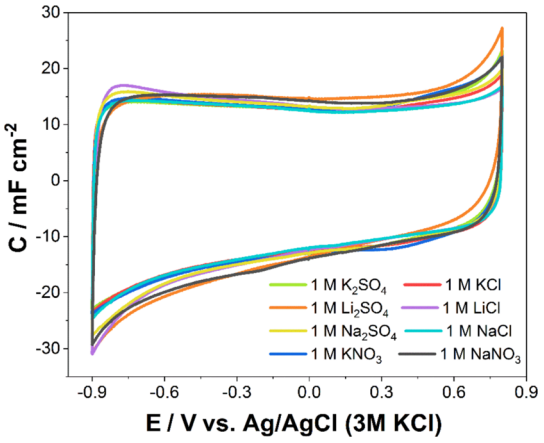

Figure 5. CV curves of the TiO_2NT−BDD electrode recorded in various electrolytes; ν = 100 mV s^{-1}.

electrode depending on the electrolyte. However, similar to study by Qu et al. there were no obvious differences among the investigated electrolytes (Li_2SO_4, Na_2SO_4 and K_2SO_4) at low scan rates.[70]

The normalized capacitance values C (mF cm^{-2}) were calculated from the relation $C = i/\nu \cdot A$, where i is the current (A), ν is the potential sweep rate (0.1 V s^{-1}), and A is the electrode surface (cm^2).[71] The capacitance of the TiO_2NT−BDD electrode is highest at the highest electrolyte concentration, reaching ∼15 mF cm^{-2}. The achieved capacitance value is almost twice as high as we previously received for a BDD layer with the [B]/[C] ratios of 10k prepared in the gas phase.[27] Furthermore, the received value is much higher than the capacitance 9.5 mF cm^{-2} obtained for other diamond-based electrodes.[72]

As previously mentioned, BDD is known for its high oxidation and reduction overpotentials in aqueous electrolytes. For this reason, the goal of the next analysis was to investigate the electrode stability with increasing anodic polarization potential. The results obtained for selected sulfate-based electrolytes are shown in Figure 6a within the polarization range of −0.9 to 1.8 V versus AglAgCl, whereas measurements for electrolytes with various anions in few selected polarization ranges are shown in Figure 6b−d.

As seen, there is no significant difference in current densities between the TiO_2NT−BDD electrodes in each tested sulfate-based electrolyte. Moreover, the studied electrodes in electrolytes containing different anions showed stability in the anodic polarization up to 1.5 V in both nitrate and sulfate solutions. For chlorides, a significantly narrower stability range is noticeable, which is related to the Cl^--to-Cl_2 electrooxidation. This means that BDD exhibits high overpotential only for a water oxidation reaction but not a chlorine evolution reaction.

Multiple galvanostatic charge−discharge tests were carried out for the TiO_2NT−BDD electrodes in two previously selected aqueous electrolytes: 1 M $NaNO_3$ and 1 M Na_2SO_4 (Figure 7). Polarization with an anodic and cathodic current gives almost identical normalized capacitance values for a potential window equal to 2.0 V in both electrolytes, indicating a reversible process of charge storage. After a test sequence of 1000 charge−discharge cycles, over 94.0 and 78.2% of the initially normalized capacitances were maintained for the TiO_2NT−BDD electrode polarized in the narrower potential window (ΔE = 2.0 V) in 1 M $NaNO_3$, and 1 M Na_2SO_4, respectively. Increasing the potential window does not translate to the capacitance increase. The capacitances calculated after charge−discharge tests for ΔE = 2.4 V were even smaller, equal to 52.0% of the initial value obtained in nitrate, and 44.4% in sulfate. These results suggest that nitrate is the more stable electrolyte in this system.

The chronopotentiometry curves observed for the narrower potential window (inset Figure 7a) reveal symmetric shape with a linear variation of voltage with time. Thus, the IR drop is negligible and the system exhibits the ideal electric double layer capacitance (EDLC). For comparison, the charge/discharge profile obtained between −0.9 and 1.5 V, in both

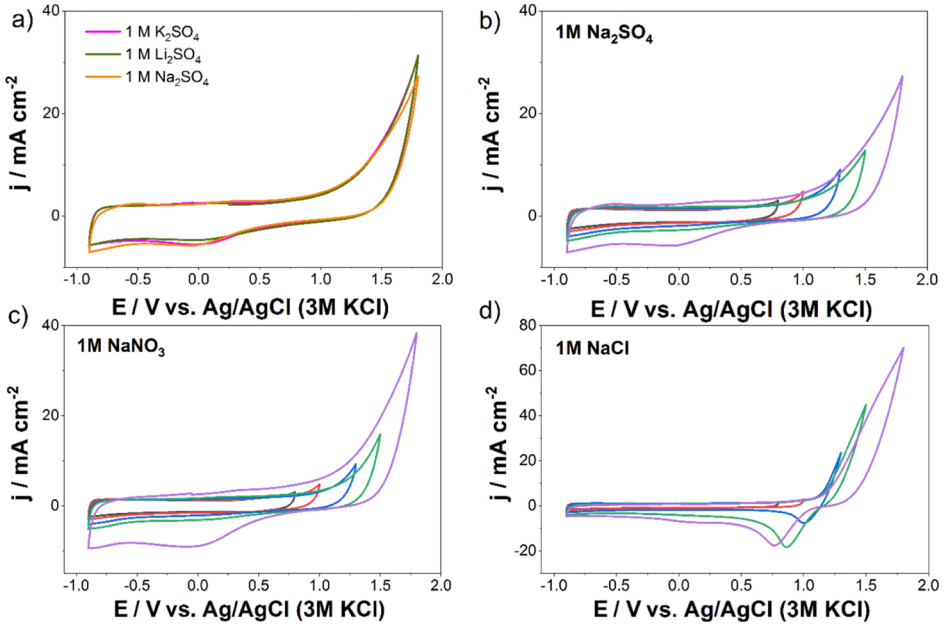

Figure 6. Current density values of the TiO_2NT−BDD electrode recorded in (a) sulfates differing in cations in the range of −0.9 ÷ 1.8 V; different polarization ranges in (b) 1 M $NaNO_3$, (c) 1 M Na_2SO_4, (d) 1 M NaCl; sweep rate 100 mV s^{-1}.

https://dx.doi.org/10.1021/acs.jpcc.0c02792
J. Phys. Chem. C 2020, 124, 15698−15712

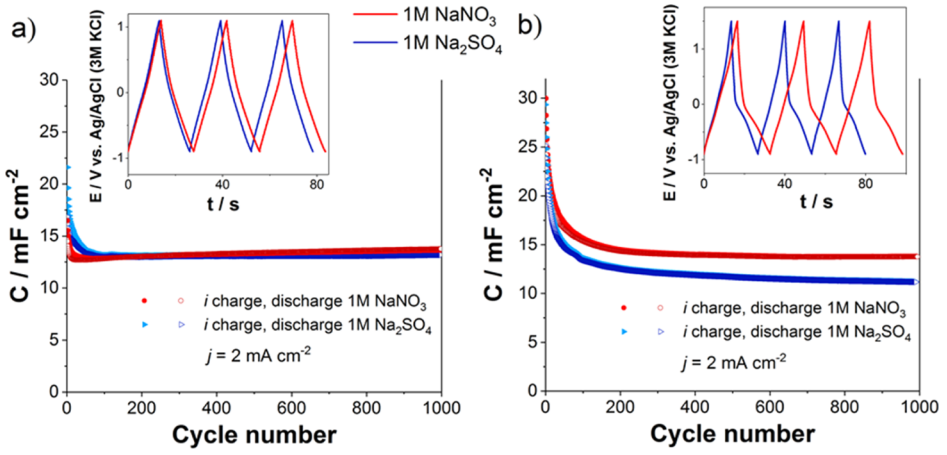

Figure 7. TiO_2NT−BDD electrode capacitance as a function of cycle number in 1 M $NaNO_3$ and 1 M Na_2SO_4 recorded in at various polarization ranges: (a) −0.9 to 1.1 V (ΔE = 2.0 V), (b) −0.9 to 1.5 V (ΔE = 2.4 V); current density: 2 mA cm^{-2}. Insets: the last cathodic and anodic branches (997−1000 cycle) of the chronopotentiometry curve.

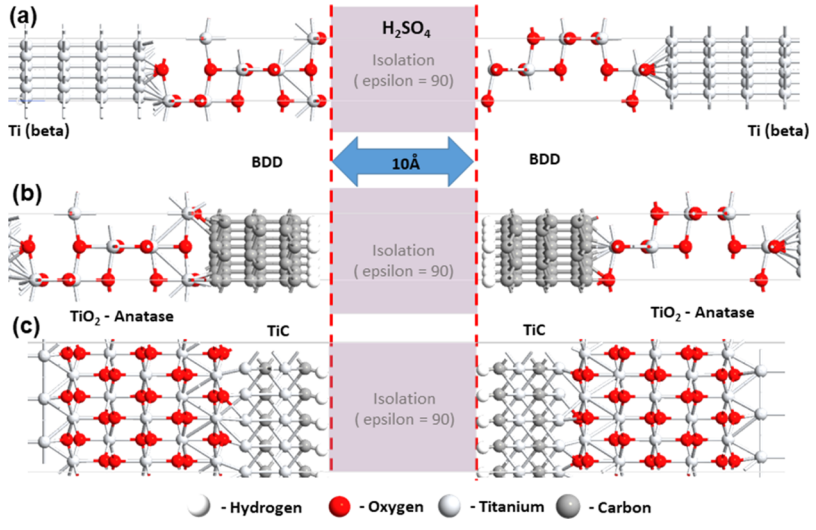

Figure 8. Specific two-electrode slabs devices: (a) reference bare TiO_2NT; (b) TiO_2NT covered by BDD and (c) TiO_2NT covered by TiC separated by H_2SO_4-based electrolyte.

electrolytes, displayed a nonlinearity, which represented the pseudocapacitance behavior resulting from a Faradic reaction, connected with the oxidation of the BDD termination layer under deep anodic polarization[73] (inset Figure 7b).

The presented results allowed a conclusion to be made regarding the various electrochemical stabilities of the investigated TiO_2NT−BDD electrodes in a wide anodic polarization range, depending on the studied electrolyte. Exceeding an anodic polarization of 1.4 V is sufficient for modification of the electrochemical performance of BDD electrodes by oxidation of the termination functional groups.[61,62,74−76] The BDD oxidation has been thoroughly studied in acidic electrolytes, where anodic polarization results in a charge transfer resistance increase and capacitance drop, as a consequence. Oxidized termination of TiO_2NT−BDD is considered as the primary factor behind the worsened electrode stability during the chronopotentiometry test.

Furthermore, deep anodic polarization seems to have a different effect on BDD electrodes depending on the studied electrolyte. Cai et al.[77] showed that the hydroxyl radical generation yield in nitrates is much lower than in the sulfate media and adsorbed nitrate anions block sites where hydroxyl radicals are formed by water oxidation. The aforementioned results were true under various anodic polarization conditions (+1.0 and +3.0 V). The consequence of hydroxyl radical generation and TiO_2NT−BDD surface oxidation is a more rapid capacitance decrease for electrodes immersed in a sulfate-containing electrolyte. Therefore, we decided to use 1 M $NaNO_3$ in further studies on the SC.

3.3. First-Principles Simulation of Diamondized Titania Nanotubes Electrodes. The first-principles modeling of fabricated here TiO_2NT−BDD SC was based on the atomic-scale simulations of a parallel plate nanocapacitor assumed,[78] applying the structural data revealed by TEM and XPS. The method applied for simulating the capacitance from first-principles is to derive the electrostatic energy and from that the QC as previously reported for graphene[79] or MoS_2.[80]

Three different "two-electrode" slab models of SC were built to conduct first-principles simulations of QC using representative electrodes: (I) bare titania nanotube at Ti substrate, (II) titania nanotubes covered by BDD and (III) titania nanotubes covered by TiC.

The as-fabricated in-experiment diamondized titania electrode could not be directly simulated because of its complexity

https://dx.doi.org/10.1021/acs.jpcc.0c02792
J. Phys. Chem. C 2020, 124, 15698−15712

and too large the atomic system for DFT simulations. Nevertheless, selected slabs configurations directly correspond to the specific cases of the experimental electrode structure (see Figure 8).

The (I) slab case (Figure 8a) was built utilizing the ideal body-centered cubic allotropic form of titanium [called Ti(β)] working as a metallic substrate, anatase (TiO_2) ad-layer simulating nanotube and spacer-separator with the dielectric constant of sulfuric acid-based electrolyte (ε = 90).

The (II) slab case consists of Ti(β), anatase ad-layer similar to slab (I) and four BDD(111) layers (see Figure 8b). Because the polycrystalline BDD electrode fabricated by CVD methods are usually dominated by (111) planes,[81] such a surface has been selected for DFT investigation QC. The reconstructed diamond surface was terminated by hydrogen atoms, and two boron atoms were placed within the second carbon layer from the top surface to approximate the Raman spectra corresponding acceptor concentration of 1×10^{21} cm^{-3} (see the Supporting Information file, Figure S2), as reported in earlier studies.[82]

The (III) slab case was designed utilizing Ti(β), anatase ad-layer analogous to slab (I) replacing BDD(111) present in the slab (II) by four TiC layers (see Figure 8c). The anatase TiO_2 was simulated as a tetragonal structure (space group, $I4_1/amd$),[83] while TiC as face-centered cubic crystal NaCl-type structure (face-centered cubic) with space group $Fm\bar{3}m$ (225).[44] The spacing between electrodes was set to 10 c5 for all the slabs. Next, the cross-section area was equal to 45.28 $c5^2$. The built "two-electrode" slab models are in agreement with Landauer–Buttker formalism[84,85] QC was derived utilizing electrostatic difference potential and differential electron density.

The simulated QC reaches values of 6.39045×10^{-21}, 7.97111×10^{-21} and 2.04258×10^{-20} F for (I), (II) and (III) slab case, respectively. Thus, BDD at titania (case II) results in 25% rise of QC, while TiC at titania (case III) delivers 320% higher QR relating to reference bare anatase (case I).

In general, the differential charge density exhibits smaller values for BDD (case II), when compared with TiC (case III) or referencing TiO_2 (case I shown in Figure 9a). In (II) case with BDD coverage (see Figure 9b), the charge is delocalized, thus, not only present narrowly to the BDD surface but then a large amount of the charge migrates into the depth of the electrode structure down to titania delivering in effect average values of QC. Analysis of charge redistribution at the BDD interface led us to conclude that holes of hydrogen-terminated BDD directly interact with the electrolyte while its electrons recombine with the excited holes of TiO_2[86] resulting in scattered charge distribution.

The significant increase of QC in case (III) corresponds to the tightly localized charge distribution in the dense interatomic structure of TiC. The major charge accumulation takes place in a very narrow region right above the surface (see Figure 9c), forming two peaks between the two outer surface atoms (Ti and C). A strong covalent interaction between two layers will result in significant accumulation of charge density, hence similar interactions were reported for Ti_2C and Ti_3C_2 used for MXENES exfoliation[87] known also as superior capacitors.[88]

3.4. Investigation of the Assembled TiO_2NT–BDD SCs. To fabricate symmetric SC cells, two identical electrodes were placed in contact with an aqueous electrolyte in a coffee bag system, as described in the Experimental Section. The

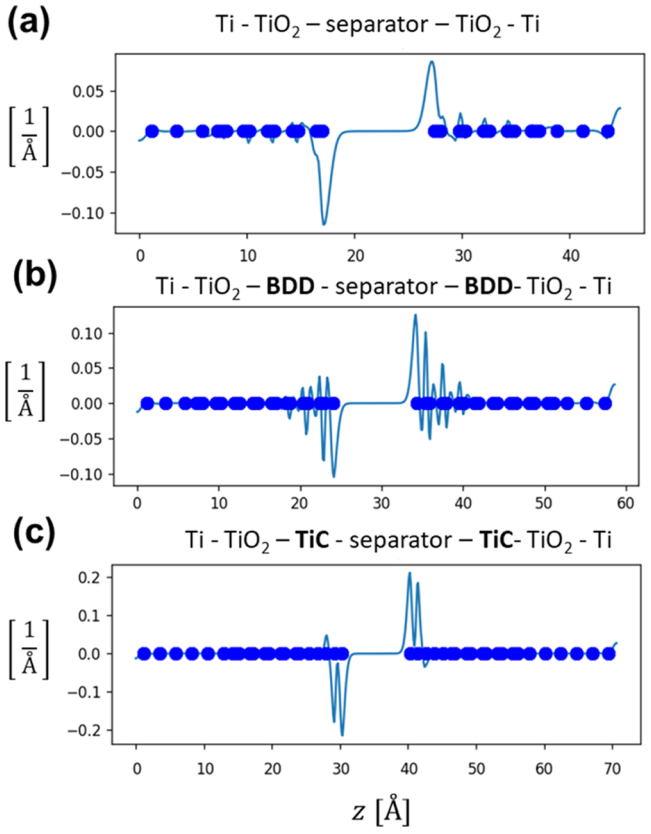

Figure 9. Charge accumulation simulated by DFT at the electrostatic potential of 1 V for: (a) reference bare TiO_2NT; (b) TiO_2NT covered by BDD, and (c) TiO_2NT covered by TiC separated by H_2SO_4-based electrolyte. Attn. The blue circles correspond to the atom positions.

photography documentation from the assembling of the investigated SCs is available in the Supporting Information Figure S1. CV was used for the electrochemical characterization of the electrode materials in a two-electrode system. First, a comparison between TiO_2NT and TiO_2NT–BDD symmetric cells was made. The CV curves registered for the TiO_2NT/TiO_2NT system, depending on the range of the applied voltage, is shown in Figure 10a. The electrochemical activity observed at low voltage can be described as a reversible electrochemical reduction of Ti^{4+} centers with simultaneous H^+ doping.[89] The low current density registered at the higher voltage region is related to the electrical double layer of the metal oxide/electrolyte interface. The TiO_2-based capacitor is characterized by good electrochemical stability even at high voltage.[90]

The CV curve of the SC built with diamondized titania electrodes is shown for comparison (see Figure 10b). A huge improvement in electrode capacitance is clearly seen. The stability range of the applied voltages seems to be diminished in comparison to unmodified electrodes because of the presence of BDD. However, BDD is known as an inhibitor of water electrooxidation,[41,52] thus it is very likely that irreversible oxidation at the high voltage region is rather related to the oxidation of sp^2 carbon residues formed during BDD deposition. Nevertheless, a voltage of 1.6 V was achieved in the studied 1 M $NaNO_3$ electrolyte.

Multiple charge–discharge cycles were performed in order to test the influence of the applied voltage on the electrochemical performance and stability of the tested SCs. The

https://dx.doi.org/10.1021/acs.jpcc.0c02792
J. Phys. Chem. C 2020, 124, 15698–15712

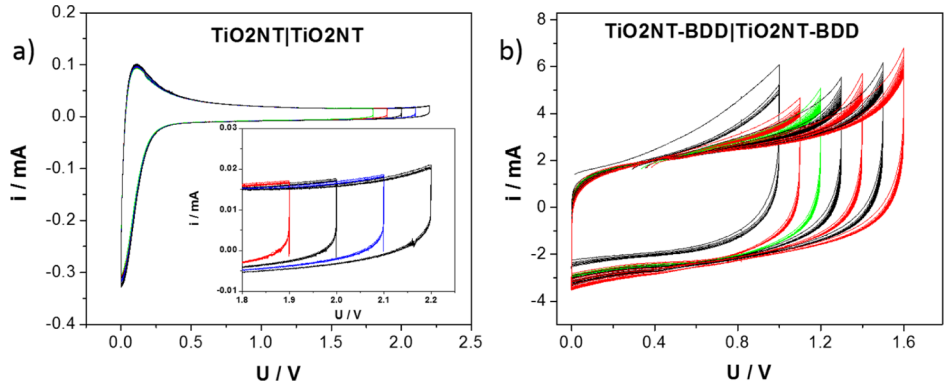

Figure 10. Comparison of CV curves recorded in a two-electrode system for bare TiO_2NT and diamondized SCs.

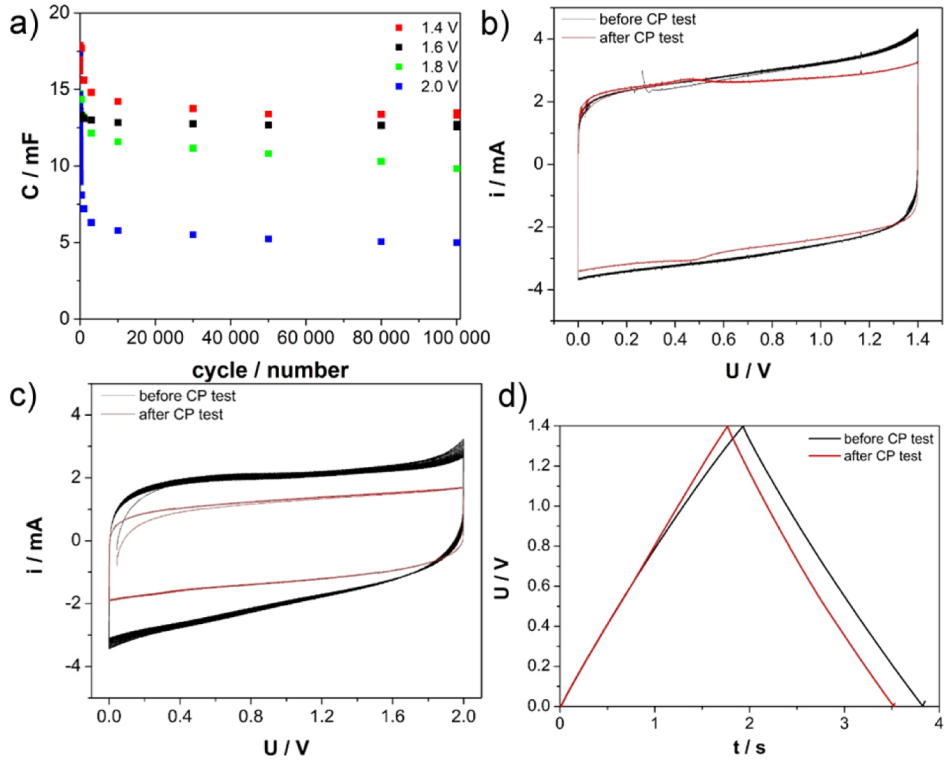

Figure 11. Results of long term electrochemical tests of TiO_2NT−BDD recorded in two-electrode symmetrical cells: (a) Capacitance vs cycle number plot; (b,c) CV curves recorded for 1.6 and 2.0 V; (d) exemplary chronopotentiometry curves for 1.6 V.

effect of 4 different ranges of applied voltage on capacitance retention is shown in Figure 11. As is shown, very good stability, even after 100k cycles, was obtained for the capacitor tested with applied voltage range to 1.6 V. The capacitance retention between the 10th and 100,000th chronopotentiometry cycle was equal to 93%. The determined capacitance retention for TiO_2NT−BDD at this voltage is superior to other hybrid SCs.[26,91] The CV curves and EIS spectra recorded at the beginning and after the electrochemical test confirm that a TiO_2NT−BDD-based SC can safely work under such conditions, see Figure 11a, and the Supporting Information file, Figure S3 and Table S1.

The extension of the limits of the polarization range negatively affects the performance of the electrochemical cells. The capacitance retention was equal to 81.2, 93.0, 69.8 and 28.5% for 1.4, 1.6, 1.8 and 2.0 V, respectively.

The effect of the capacitance drop was also tracked using CV and chronopotentiometry. The curves recorded before and after a long-term charging test are shown in Figure 11b−d. It is noteworthy that the decrease of capacitance is the highest at the beginning of the charge−discharge tests, and then the capacitance stabilized after approx. 10,000 cycles. In the case of a multi-component electrode system, the total capacitance originates from both EDLC as well as pseudofaradaic capacitance (PC). Because the CV curves exhibit almost perfect rectangular shape and there are no clear redox peaks visible, the EDLC contribution is probably much higher. However, the electrode material may exhibit Faradaic reactions related to redox of Ti centers in TiO_2 and changes of the BDD surface termination. The EDLC capacitors are generally characterized by much higher stability than PC.[92] Additionally, our system works in an aqueous electrolyte. Despite the fact that in the organic electrolyte the higher operating voltages may be achieved, the presence of organic solvent may negatively affect the electrode stability during multiple charge−discharge cycles in comparison to the water-based

https://dx.doi.org/10.1021/acs.jpcc.0c02792
J. Phys. Chem. C 2020, 124, 15698−15712

electrolyte as it was previously reported.[53] Thus, in the case of TiO_2NT−BDD tested in a more narrow potential range (1.4 and 1.6 V), the electrodes exhibits almost perfect stability because mainly the EDLC is used. At the same time the electroactive BDD surface affecting PC does not change, or changes in a reversible fashion. In the case of the higher operating voltage (1.8 and 2 V), the BDD surface termination may be irreversibly oxidized, causing capacitance drop. Changes in the BDD surface are reported to affect the electrode electrochemical performance.[93] The observed interface modification is unfavorable for energy storage devices and leads to lower capacitance retention rates. The tested cells exhibit energy storage ability even in the 2.0 V range; however, because of the poor capacitance retention, capacitances are significantly lower. Thus, the modification of titania nanotubes with BDD, leading to the formation of titania carbide clusters allows electrode materials to be prepared that can work in symmetric cells up to 2.0 V in aqueous electrolytes; however, to achieve good electrochemical stability, the voltage should not exceed 1.6 V.

The specific energy density E_g (W h kg^{-1}) was determined according to the relation eq 1[94,95]

$$E_n = C \cdot V^2/2 \cdot m \quad (1)$$

where C is the capacitance (F), V the applied voltage (V), m the mass of the active material (kg). The specific power density P_g (kW kg^{-1}) is given by eq 2[96,97]

$$P_g = E_n/\Delta t_{dis} \quad (2)$$

where Δt_{dis} is discharge time. In order to calculate these parameters, one must estimate the mass loading of the active electrode material. As pointed out by Gogotsi and Simon,[98] the exceptional performance of nanomaterial-based SCs results from very low active material weight, while the performance significantly declines in highly loaded electrodes. Nevertheless, the aforementioned approach offers the best method of direct energy density comparison between various electrode materials. The mass of the TiO_2NT−BDD was 0.375 mg, excluding TiO_2.

The gravimetric capacitance of the studied symmetric TiO_2NT−BDD SC was 41.47 F g^{-1} (for the capacitor tested to 1.6 V). It should also be noted that the energy/power density can only be used to characterize the electrochemical profile of a SC device, rather than a single electrode.[89] The highest values for energy density and power density calculated at a current density of 3 A g^{-1} were 14.74 W h kg^{-1} and 24.68 kW kg^{-1}, respectively.[99] The maximum power density of TiO_2NT−BDD SC is either much higher or similar, compared to the values recently reported for other TiO_2,[100,101] TiC,[102,103] BDD,[12,53] or graphene[104−107] based SCs with similar energy densities. Moreover, the maximum energy density calculated for TiO_2NT−BDD SC is similar to other previously reported devices, however it is reached at up to 10 times lower power density, making our SC much more efficient.[97,108,109] The graphical representation of chosen recently reported SCs performance is presented in the Supporting Information (Figure S4). In order to further improve material properties, it is essential to obtain high volume of active nanomaterial, which may be achieved aiming at novel materials with high surface area and hierarchical porosity.[110,111] High measured capacitance originates from the titania carbide growths on titania nanotubes. In order to address higher volumetric energy densities our next focus is nanocomposite geometry and optimization of process conditions, aiming for more homogeneous and dense distribution of TiC nanoparticles, but also manipulating TiO_2NT thickness and pore diameter.

4. CONCLUSIONS

In summary, the composite TiO_2NT−BDD electrodes were fabricated utilizing specific combination of anodization followed by CVD resulting in high-performance capacitive effect. The specific plasma composition and CVD process chemistry induces diamondization of titania nanotubes resulting in simultaneous growth of complex BDD/TiC interface. It was found that high capacitance phenomena is delivered by nanoporous, multi-faceted and substoichiometric TiC, forming clusters at the lateral surfaces of titania nanotubes. Next, the brittle TiC interface is protected by highly conductive although discontinuous BDD overlayer providing also effective charge transfer at the electrode−electrolyte barrier. The first-principles simulations manifested 320% increase of titania/TiC nanostructures attributed to the tightly localized charge distribution in a very narrow region right above the TiC surface.

Recent works manifested that TiC is formed by the transformation of TiO_2 to Ti_2O_3, while our BF-TEM studies showed that nano-cylindrical and multi-faceted TiC clusters are nucleated by surfaces defect at the inter-tubular interfaces of TiO@NT array. On this basis, the detailed molecular growth mechanism Ti−C formation at the interface of TiO_2NT−BDD composite was proposed.

The assembled two-electrode SC devices exhibited capacitance 15 mF cm^{-2} at 0.1 V s^{-1} of the scan rate. The TiO_2NT−BDD electrodes allows for work in symmetric cells up to 2.0 V in aqueous electrolytes to be prepared, however to achieve good electrochemical stability, the voltage cannot exceed 1.6 V.

Designed SCs were characterized by outstanding long-term cycling stability with capacitance retention of 93% after 100,000 chronopotentiometric cycles, overwhelming the drawback of capacitance retention of bare TiC electrodes. The electrode capacitive behavior as well as the stability is primarily attributed to formation of hydroxyl radicals on the BDD electrode surface, with the consequence of surface passivation at higher anodic polarization potentials.

Based on the experimental findings, we have achieved remarkably high energy density of 14.74 W h kg^{-1} and a power density of 24.68 kW kg^{-1}, measured in two-electrode conditions of the operating SC cell.

The novel diamondized titania nanocomposite SCs delivers both high power and energy densities with high capacitance retention rates allowing for work with aqueous electrolytes without polymeric binders necessary for standard amorphous carbon SCs.

■ ASSOCIATED CONTENT

Supporting Information

The Supporting Information is available free of charge at https://pubs.acs.org/doi/10.1021/acs.jpcc.0c02792.

Procedure of assembling of TiO_2NT−BDD SCs; Raman spectra maps of TiO_2NT−BDD composite electrodes; EIS studies of the SC before and after 100,000 charge−discharge cycles; and power/energy densities comparison of recently reported SCs (PDF)

https://dx.doi.org/10.1021/acs.jpcc.0c02792
J. Phys. Chem. C 2020, 124, 15698−15712

AUTHOR INFORMATION

Corresponding Authors

Robert Bogdanowicz − *Gdańsk University of Technology, 80-233 Gdańsk, Poland;* orcid.org/0000-0002-7543-2620; Email: rbogdan@eti.pg.edu.pl

Jacek Ryl − *Gdańsk University of Technology, 80-233 Gdańsk, Poland;* orcid.org/0000-0002-0247-3851; Email: jacek.ryl@pg.edu.pl

Authors

Anna Dettlaff − *Gdańsk University of Technology, 80-233 Gdańsk, Poland;* orcid.org/0000-0002-5631-950X

Franciszek Skiba − *DI4MAN sp. z o.o. ul., 18-400 Łomża, Poland*

Konrad Trzcinski − *Gdańsk University of Technology, 80-233 Gdańsk, Poland*

Mariusz Szkoda − *Gdańsk University of Technology, 80-233 Gdańsk, Poland;* orcid.org/0000-0001-6590-0278

Michal Sobaszek − *Gdańsk University of Technology, 80-233 Gdańsk, Poland;* orcid.org/0000-0002-3180-9297

Mateusz Ficek − *Gdańsk University of Technology, 80-233 Gdańsk, Poland*

Bartlomiej Dec − *Gdańsk University of Technology, 80-233 Gdańsk, Poland*

Lukasz Macewicz − *Gdańsk University of Technology, 80-233 Gdańsk, Poland*

Konrad Wyrębski − *Technical University of Liberec, 461 17 Liberec, Czech Republic*

Grzegorz Pasciak − *Institute of Low Temperature and Structure Research, Polish Academy of Sciences, 50-950 Wroclaw, Poland*

Dongsheng Geng − *Beijing Key Laboratory for Magneto-Photoelectrical Composite and Interface Science, School of Mathematics and Physics, University of Science and Technology Beijing, Beijing 100083, China;* orcid.org/0000-0003-0910-8985

Arkadiusz Ignaczak − *DI4MAN sp. z o.o. ul., 18-400 Łomża, Poland*

Complete contact information is available at: https://pubs.acs.org/10.1021/acs.jpcc.0c02792

Notes

The authors declare no competing financial interest.

ACKNOWLEDGMENTS

The authors gratefully acknowledge financial support in parts from the Polish National Science Centre (NCN) under grant no. 2015/17/D/ST5/02571 and the National Centre for Science and Development grant no. POIR.01.01.01-00-0834/16-00. The DS funds of the Faculty of Electronics, Telecommunications and Informatics of the Gdańsk University of Technology are also acknowledged.

REFERENCES

(1) Eftekhari, A. Lithium Batteries for Electric Vehicles: From Economy to Research Strategy. *ACS Sustainable Chem. Eng.* **2019**, *7*, 5602−5613.

(2) Eftekhari, A.; Mohamedi, M. Tailoring Pseudocapacitive Materials from a Mechanistic Perspective. *Mater. Today Energy* **2017**, *6*, 211−229.

(3) Lee, K.; Mazare, A.; Schmuki, P. One-Dimensional Titanium Dioxide Nanomaterials: Nanotubes. *Chem. Rev.* **2014**, *114*, 9385−9454.

(4) Zhou, H.; Zhang, Y. Electrochemically Self-Doped TiO $_2$ Nanotube Arrays for Supercapacitors. *J. Phys. Chem. C* **2014**, *118*, 5626−5636.

(5) Wu, H.; Li, D.; Zhu, X.; Yang, C.; Liu, D.; Chen, X.; Song, Y.; Lu, L. High-Performance and Renewable Supercapacitors Based on TiO2 Nanotube Array Electrodes Treated by an Electrochemical Doping Approach. *Electrochim. Acta* **2014**, *116*, 129−136.

(6) Chen, J.; Xia, Z.; Li, H.; Li, Q.; Zhang, Y. Preparation of Highly Capacitive Polyaniline/Black TiO 2 Nanotubes as Supercapacitor Electrode by Hydrogenation and Electrochemical Deposition. *Electrochim. Acta* **2015**, *166*, 174−182.

(7) Wang, Q.; Wen, Z.; Li, J. Carbon Nanotubes/TiO2 Nanotubes Hybrid Supercapacitor. *J. Nanosci. Nanotechnol.* **2007**, *7*, 3328−3331.

(8) Yu, S.; Yang, N.; Vogel, M.; Mandal, S.; Williams, O. A.; Jiang, S.; Schönherr, H.; Yang, B.; Jiang, X. Battery-like Supercapacitors from Vertically Aligned Carbon Nanofiber Coated Diamond: Design and Demonstrator. *Adv. Energy Mater.* **2018**, *8*, 1702947.

(9) Lu, X.; Wang, G.; Zhai, T.; Yu, M.; Gan, J.; Tong, Y.; Li, Y. Hydrogenated TiO $_2$ Nanotube Arrays for Supercapacitors. *Nano Lett.* **2012**, *12*, 1690−1696.

(10) Raj, C. C.; Prasanth, R. Review—Advent of TiO2 Nanotubes as Supercapacitor Electrode. *J. Electrochem. Soc.* **2018**, *165*, E345−E358.

(11) Salari, M.; Aboutalebi, S. H.; Konstantinov, K.; Liu, H. K. A Highly Ordered Titania Nanotube Array as a Supercapacitor Electrode. *Phys. Chem. Chem. Phys.* **2011**, *13*, 5038.

(12) Wang, J.; He, Z.; Tan, X.; Wang, T.; Liu, L.; He, X.; Liu, X. D.; Zhang, L.; Du, K. High-Performance 2.6 V Aqueous Symmetric Supercapacitor Based on Porous Boron Doped Diamond via Regrowth of Diamond Nanoparticles. *Carbon* **2020**, *160*, 71−79.

(13) Lu, X.; Wang, G.; Zhai, T.; Yu, M.; Gan, J.; Tong, Y.; Li, Y. Hydrogenated TiO $_2$ Nanotube Arrays for Supercapacitors. *Nano Lett.* **2012**, *12*, 1690−1696.

(14) Wu, H.; Xu, C.; Xu, J.; Lu, L.; Fan, Z.; Chen, X.; Song, Y.; Li, D. Enhanced Supercapacitance in Anodic TiO $_2$ Nanotube Films by Hydrogen Plasma Treatment. *Nanotechnology* **2013**, *24*, 455401.

(15) Shao, Z.; Li, H.; Li, M.; Li, C.; Qu, C.; Yang, B. Fabrication of Polyaniline Nanowire/TiO2 Nanotube Array Electrode for Supercapacitors. *Energy* **2015**, *87*, 578−585.

(16) Wu, H.; Xu, C.; Xu, J.; Lu, L.; Fan, Z.; Chen, X.; Song, Y.; Li, D. Enhanced Supercapacitance in Anodic TiO2nanotube Films by Hydrogen Plasma Treatment. *Nanotechnology* **2013**, *24*, 455401.

(17) Ponnamma, D.; Vijayan P, P.; Al Ali Al-Maadeed, M. 3D Architectures of Titania Nanotubes and Graphene with Efficient Nanosynergy for Supercapacitors. *Mater. Des.* **2017**, *117*, 203−212.

(18) Xiao, H.; Guo, W.; Sun, B.; Pei, M.; Zhou, G. Mesoporous TiO2 and Co-Doped TiO2 Nanotubes/Reduced Graphene Oxide Composites as Electrodes for Supercapacitors. *Electrochim. Acta* **2016**, *190*, 104−117.

(19) Eftekhari, A. Metrics for Fast Supercapacitors as Energy Storage Devices. *ACS Sustainable Chem. Eng.* **2019**, *7*, 3688−3691.

(20) Eftekhari, A. High-Energy Aqueous Lithium Batteries. *Adv. Energy Mater.* **2018**, *8*, 1801156.

(21) Zhang, J.; Yu, X.; Zhang, Z.; Li, J.; Zhao, Z.-Y. Adjusting Pore Size and Shape to Achieve the Desired Capacitance of Boron-Doped Diamond Electrodes. *Surf. Rev. Lett.* **2019**, *26*, 1830009.

(22) Zhang, J.; Yu, X.; Zhang, Z.-Q.; Zhao, Z.-Y. Preparation of Boron-Doped Diamond Foam Film for Supercapacitor Applications. *Appl. Surf. Sci.* **2020**, *506*, 144645.

(23) Lukatskaya, M. R.; Mashtalir, O.; Ren, C. E.; Dall'Agnese, Y.; Rozier, P.; Taberna, P. L.; Naguib, M.; Simon, P.; Barsoum, M. W.; Gogotsi, Y. Cation Intercalation and High Volumetric Capacitance of Two-Dimensional Titanium Carbide. *Science* **2013**, *341*, 1502−1505.

(24) Xia, X.; Zhang, Y.; Chao, D.; Xiong, Q.; Fan, Z.; Tong, X.; Tu, J.; Zhang, H.; Fan, H. J. Tubular TiC Fibre Nanostructures as Supercapacitor Electrode Materials with Stable Cycling Life and Wide-Temperature Performance. *Energy Environ. Sci.* **2015**, *8*, 1559−1568.

(25) Gao, Y.; Presser, V.; Zhang, L.; Niu, J. J.; McDonough, J. K.; Pérez, C. R.; Lin, H.; Fong, H.; Gogotsi, Y. High Power

Supercapacitor Electrodes Based on Flexible TiC-CDC Nano-Felts. *J. Power Sources* **2012**, *201*, 368−375.
(26) Xu, J.; Yang, N.; Heuser, S.; Yu, S.; Schulte, A.; Schönherr, H.; Jiang, X. Achieving Ultrahigh Energy Densities of Supercapacitors with Porous Titanium Carbide/Boron-Doped Diamond Composite Electrodes. *Adv. Energy Mater.* **2019**, *9*, 1803623.
(27) Siuzdak, K.; Bogdanowicz, R.; Sawczak, M.; Sobaszek, M. Enhanced Capacitance of Composite TiO 2 Nanotube/Boron-Doped Diamond Electrodes Studied by Impedance Spectroscopy. *Nanoscale* **2015**, *7*, 551−558.
(28) Sholl, D.; Steckel, J. A. *Density Functional Theory: A Practical Introduction*; John Wiley & Sons, 2011.
(29) Griebel, M.; Hamaekers, J. Molecular Dynamics Simulations of the Elastic Moduli of Polymer−Carbon Nanotube Composites. *Comput. Methods Appl. Mech. Eng.* **2004**, *193*, 1773−1788.
(30) Griebel, M.; Knapek, S.; Zumbusch, G. *Numerical Simulation in Molecular Dynamics: Numerics, Algorithms, Parallelization, Applications*; Springer Science & Business Media, 2007.
(31) Xu, J.; Jia, C.; Cao, B.; Zhang, W. F. Electrochemical Properties of Anatase TiO2 Nanotubes as an Anode Material for Lithium-Ion Batteries. *Electrochim. Acta* **2007**, *52*, 8044−8047.
(32) Ferrari, A. C.; Robertson, J. Interpretation of Raman Spectra of Disordered and Amorphous Carbon. *Phys. Rev. B: Condens. Matter Mater. Phys.* **2000**, *61*, 14095−14107.
(33) Hu, L.; Huo, K.; Chen, R.; Gao, B.; Fu, J.; Chu, P. K. Recyclable and High-Sensitivity Electrochemical Biosensing Platform Composed of Carbon-Doped TiO2 Nanotube Arrays. *Anal. Chem.* **2011**, *83*, 8138−8144.
(34) Vijayan, B. K.; Dimitrijevic, N. M.; Finkelstein-Shapiro, D.; Wu, J.; Gray, K. A. Coupling Titania Nanotubes and Carbon Nanotubes To Create Photocatalytic Nanocomposites. *ACS Catal.* **2012**, *2*, 223−229.
(35) Sawczak, M.; Sobaszek, M.; Siuzdak, K.; Ryl, J.; Bogdanowicz, R.; Darowicki, K.; Gazda, M.; Cenian, A. Formation of Highly Conductive Boron-Doped Diamond on TiO $_2$ Nanotubes Composite for Supercapacitor or Energy Storage Devices. *J. Electrochem. Soc.* **2015**, *162*, A2085−A2092.
(36) Lohse, B. H.; Calka, A.; Wexler, D. Raman Spectroscopy Sheds New Light on TiC Formation during the Controlled Milling of Titanium and Carbon. *J. Alloys Compd.* **2007**, *434*−*435*, 405−409.
(37) Sobaszek, M.; Siuzdak, K.; Sawczak, M.; Ryl, J.; Bogdanowicz, R. Fabrication and Characterization of Composite TiO2 Nanotubes/Boron-Doped Diamond Electrodes towards Enhanced Supercapacitors. *Thin Solid Films* **2016**, *601*, 35−40.
(38) Zemek, J.; Houdkova, J.; Jiricek, P.; Jelinek, M. Amorphous Carbon Nanocomposite Films Doped by Titanium: Surface and Sub-Surface Composition and Bonding. *Diamond Relat. Mater.* **2018**, *81*, 61−69.
(39) Lu, Y.-G.; Turner, S.; Verbeeck, J.; Janssens, S. D.; Wagner, P.; Haenen, K.; Van Tendeloo, G. Direct Visualization of Boron Dopant Distribution and Coordination in Individual Chemical Vapor Deposition Nanocrystalline B-Doped Diamond Grains. *Appl. Phys. Lett.* **2012**, *101*, 041907.
(40) Siuzdak, K.; Szkoda, M.; Lisowska-Oleksiak, A.; Grochowska, K.; Karczewski, J.; Ryl, J. Thin Layer of Ordered Boron-Doped TiO 2 Nanotubes Fabricated in a Novel Type of Electrolyte and Characterized by Remarkably Improved Photoactivity. *Appl. Surf. Sci.* **2015**, *357*, 942−950.
(41) Godbole, V. P.; Kim, G. S.; Dar, M. A.; Kim, Y. S.; Seo, H. K.; Khang, G.; Shin, H. S. Hot Filament Chemical Vapour Deposition Processing of Titanate Nanotube Coatings. *Nanotechnology* **2005**, *16*, 1186−1191.
(42) Sawczak, M.; Sobaszek, M.; Siuzdak, K.; Ryl, J.; Bogdanowicz, R.; Darowicki, K.; Gazda, M.; Cenian, A. Formation of Highly Conductive Boron-Doped Diamond on TiO2 Nanotubes Composite for Supercapacitor or Energy Storage Devices. *J. Electrochem. Soc.* **2015**, *162*, A2085−A2092.
(43) Gusev, A. I.; Rempel, A. A. *Nanocrystalline Materials*, 1st ed.; Cambridge International Science Publishing Ltd.: Cambridge, 2003.
(44) Wyckoff, R. W. G. *Crystal Structures*, 2nd ed.; Wiley, 1963; Vol. *1*.
(45) Dahlqvist, M.; Alling, B.; Abrikosov, I. A.; Rosén, J. Phase Stability of Ti 2 AlC upon Oxygen Incorporation: A First-Principles Investigation. *Phys. Rev. B: Condens. Matter Mater. Phys.* **2010**, *81*, 024111.
(46) Jalili, S.; Molani, F.; Schofield, J. Ti-Coated BC $_2$ N Nanotubes as Hydrogen Storage Materials. *Can. J. Chem.* **2013**, *91*, 598−604.
(47) Hugosson, H. W.; Korzhavyi, P.; Jansson, U.; Johansson, B.; Eriksson, O. Phase Stabilities and Structural Relaxations in Substoichiometric ${\mathrm{TiC}}_{1\ensuremath{-}x}$. *Phys. Rev. B: Condens. Matter Mater. Phys.* **2001**, *63*, 165116.
(48) Chmiola, J. Anomalous Increase in Carbon Capacitance at Pore Sizes Less Than 1 Nanometer. *Science* **2006**, *313*, 1760−1763.
(49) Jäckel, N.; Simon, P.; Gogotsi, Y.; Presser, V. Increase in Capacitance by Subnanometer Pores in Carbon. *ACS Energy Lett.* **2016**, *1*, 1262−1265.
(50) Luo, Y.-R. *Comprehensive Handbook of Chemical Bond Energies*, 1st ed.; CRC Press, 2007.
(51) Bogdanowicz, R.; Gnyba, M.; Wroczy, P.; Kosmowski, B. B. Optoelectronic System for Monitoring of Thin Diamond Layers Growth. *J. Optoelectron. Adv. Mater.* **2010**, *12*, 1660.
(52) Speight, J. *Lange's Handbook of Chemistry*, 70th Anniversary Edition, 16 ed.; McGraw-Hill Education: New York, 2005.
(53) Xu, J.; Yang, N.; Heuser, S.; Yu, S.; Schulte, A.; Schönherr, H.; Jiang, X. Achieving Ultrahigh Energy Densities of Supercapacitors with Porous Titanium Carbide/Boron-Doped Diamond Composite Electrodes. *Adv. Energy Mater.* **2019**, *9*, 1803623.
(54) An, H.-R.; Park, S. Y.; Kim, H.; Lee, C. Y.; Choi, S.; Lee, S. C.; Seo, S.; Park, E. C.; Oh, Y.-K.; Song, C.-G.; Won, J.; Kim, Y. J.; Lee, J.; Lee, H. U.; Lee, Y.-C. Advanced Nanoporous TiO 2 Photocatalysts by Hydrogen Plasma for Efficient Solar-Light Photocatalytic Application. *Sci. Rep.* **2016**, *6*, 29683.
(55) Létiche, M.; Brousse, K.; Demortière, A.; Huang, P.; Daffos, B.; Pinaud, S.; Respaud, M.; Chaudret, B.; Roussel, P.; Buchaillot, L.; Taberna, P. L.; Simon, P.; Lethien, C. Sputtered Titanium Carbide Thick Film for High Areal Energy on Chip Carbon-Based Micro-Supercapacitors. *Adv. Funct. Mater.* **2017**, *27*, 1606813.
(56) Simon, P.; Gogotsi, Y. Charge Storage Mechanism in Nanoporous Carbons and Its Consequence for Electrical Double Layer Capacitors. *Philos. Trans. R. Soc., A* **2010**, *368*, 3457−3467.
(57) Lin, S.-Y.; Zhang, X. Two-Dimensional Titanium Carbide Electrode with Large Mass Loading for Supercapacitor. *J. Power Sources* **2015**, *294*, 354−359.
(58) Scanlon, D. O.; Dunnill, C. W.; Buckeridge, J.; Shevlin, S. A.; Logsdail, A. J.; Woodley, S. M.; Catlow, C. R. A.; Powell, M. J.; Palgrave, R. G.; Parkin, I. P.; Watson, G. W.; Keal, T. W.; Sherwood, P.; Walsh, A.; Sokol, A. A. Band Alignment of Rutile and Anatase TiO2. *Nat. Mater.* **2013**, *12*, 798−801.
(59) Li, S.-C.; Diebold, U. Reactivity of TiO $_2$ Rutile and Anatase Surfaces toward Nitroaromatics. *J. Am. Chem. Soc.* **2010**, *132*, 64−66.
(60) Zhang, J.; Yan, S.; Fu, L.; Wang, F.; Yuan, M.; Luo, G.; Xu, Q.; Wang, X.; Li, C. Photocatalytic Degradation of Rhodamine B on Anatase, Rutile, and Brookite TiO2. *Chin. J. Catal.* **2011**, *32*, 983−991.
(61) Ryl, J.; Burczyk, L.; Bogdanowicz, R.; Sobaszek, M.; Darowicki, K. Study on Surface Termination of Boron-Doped Diamond Electrodes under Anodic Polarization in H 2 SO 4 by Means of Dynamic Impedance Technique. *Carbon* **2016**, *96*, 1093−1105.
(62) Ryl, J.; Burczyk, L.; Zielinski, A.; Ficek, M.; Franczak, A.; Bogdanowicz, R.; Darowicki, K. Heterogeneous Oxidation of Highly Boron-Doped Diamond Electrodes and Its Influence on the Surface Distribution of Electrochemical Activity. *Electrochim. Acta* **2019**, *297*, 1018−1027.
(63) Haryński, Ł.; Grochowska, K.; Karczewski, J.; Ryl, J.; Siuzdak, K. Scalable Route toward Superior Photoresponse of UV-Laser-Treated TiO2 Nanotubes. *ACS Appl. Mater. Interfaces* **2020**, *12*, 3225−3235.

https://dx.doi.org/10.1021/acs.jpcc.0c02792
J. Phys. Chem. C 2020, 124, 15698−15712

(64) Lewin, E.; Persson, P. O. c5.; Lattemann, M.; Stüber, M.; Gorgoi, M.; Sandell, A.; Ziebert, C.; Schäfers, F.; Braun, W.; Halbritter, J.; Ulrich, S.; Eberhardt, W.; Hultman, L.; Siegbahn, H.; Svensson, S.; Jansson, U. On the Origin of a Third Spectral Component of C1s XPS-Spectra for Nc-TiC/a-C Nanocomposite Thin Films. *Surf. Coat. Technol.* **2008**, *202*, 3563−3570.
(65) Parra, E. R.; Arango, P. J. A.; Palacio, V. J. B. Xps Structure Analysis Of Tin/Tic Bilayers Produced By Pulsed Vacuum Arc Discharge. *DYNA* **2010**, *77*, 64.
(66) Lewin, E.; André, B.; Urbonaite, S.; Wiklund, U.; Jansson, U. Synthesis, Structure and Properties of Ni-Alloyed TiCx -Based Thin Films. *J. Mater. Chem.* **2010**, *20*, 5950−5960.
(67) Pham, V. H.; Nguyen-Phan, T.-D.; Tong, X.; Rajagopalan, B.; Chung, J. S.; Dickerson, J. H. Hydrogenated TiO2@reduced Graphene Oxide Sandwich-like Nanosheets for High Voltage Supercapacitor Applications. *Carbon* **2018**, *126*, 135−144.
(68) Bogdanowicz, R.; Fabiańska, A.; Golunski, L.; Sobaszek, M.; Gnyba, M.; Ryl, J.; Darowicki, K.; Ossowski, T.; Janssens, S. D.; Haenen, K.; Siedlecka, E. M. Influence of the Boron Doping Level on the Electrochemical Oxidation of the Azo Dyes at Si/BDD Thin Film Electrodes. *Diamond Relat. Mater.* **2013**, *39*, 82−88.
(69) Bichat, M. P.; Raymundo-Piñero, E.; Béguin, F. High Voltage Supercapacitor Built with Seaweed Carbons in Neutral Aqueous Electrolyte. *Carbon* **2010**, *48*, 4351−4361.
(70) Qu, Q. T.; Wang, B.; Yang, L. C.; Shi, Y.; Tian, S.; Wu, Y. P. Study on Electrochemical Performance of Activated Carbon in Aqueous Li2SO4, Na2SO4 and K2SO4 Electrolytes. *Electrochem. Commun.* **2008**, *10*, 1652−1655.
(71) Dettlaff, A.; Das, P. R.; Komsiyska, L.; Osters, O.; Łuczak, J.; Wilamowska-Zawłocka, M. Electrode Materials for Electrochemical Capacitors Based on Poly(3,4 Ethylenedioxythiophene) and Functionalized Multi-Walled Carbon Nanotubes Characterized in Aqueous and Aprotic Electrolytes. *Synth. Met.* **2018**, *244*, 80−91.
(72) Siuzdak, K.; Bogdanowicz, R. Nano-Engineered Diamond-Based Materials for Supercapacitor Electrodes: A Review. *Energy Technol.* **2018**, *6*, 223−237.
(73) Ryl, J.; Burczyk, L.; Bogdanowicz, R.; Sobaszek, M.; Darowicki, K. Study on Surface Termination of Boron-Doped Diamond Electrodes under Anodic Polarization in H2SO4 by Means of Dynamic Impedance Technique. *Carbon* **2016**, *96*, 1093−1105.
(74) Ryl, J.; Zielinski, A.; Bogdanowicz, R.; Darowicki, K. Heterogeneous Distribution of Surface Electrochemical Activity in Polycrystalline Highly Boron-Doped Diamond Electrodes under Deep Anodic Polarization. *Electrochem. Commun.* **2017**, *83*, 41−45.
(75) Ivandini, T. A.; Watanabe, T.; Matsui, T.; Ootani, Y.; Iizuka, S.; Toyoshima, R.; Kodama, H.; Kondoh, H.; Tateyama, Y.; Einaga, Y. Influence of Surface Orientation on Electrochemical Properties of Boron-Doped Diamond. *J. Phys. Chem. C* **2019**, *123*, 5336−5344.
(76) Simon, N.; Girard, H.; Ballutaud, D.; Ghodbane, S.; Deneuville, A.; Herlem, M.; Etcheberry, A. Effect of H and O Termination on the Charge Transfer of Moderately Boron Doped Diamond Electrodes. *Diamond Relat. Mater.* **2005**, *14*, 1179−1182.
(77) Cai, J.; Niu, T.; Shi, P.; Zhao, G. Boron-Doped Diamond for Hydroxyl Radical and Sulfate Radical Anion Electrogeneration, Transformation, and Voltage-Free Sustainable Oxidation. *Small* **2019**, *15*, 1900153.
(78) Atomic-scale capacitance|QuantumATK Q-2019.12 Documentation https://docs.quantumatk.com/tutorials/atomic-scale_capacitance/atomic-scale_capacitance.html (accessed Feb 21, 2020).
(79) Yang, G. M.; Zhang, H. Z.; Fan, X. F.; Zheng, W. T. Density Functional Theory Calculations for the Quantum Capacitance Performance of Graphene-Based Electrode Material. *J. Phys. Chem. C* **2015**, *119*, 6464−6470.
(80) Xu, Q.; Yang, G. M.; Zheng, W. T. DFT Calculation for Stability and Quantum Capacitance of MoS2 Monolayer-Based Electrode Materials. *Mater. Today Commun.* **2020**, *22*, 100772.
(81) Ekimov, E. A.; Sidorov, V. A.; Bauer, E. D.; Mel'nik, N. N.; Curro, N. J.; Thompson, J. D.; Stishov, S. M. Superconductivity in Diamond. *Nature* **2004**, *428*, 542−545.
(82) Zhao, S.; Larsson, K. Theoretical Study of the Energetic Stability and Geometry of Terminated and B-Doped Diamond (111) Surfaces. *J. Phys. Chem. C* **2014**, *118*, 1944−1957.
(83) Horn, M.; Schwebdtfeger, C. F.; Meagher, E. P. Refinement of the Structure of Anatase at Several Temperatures. *Z. Kristallogr. - Cryst. Mater.* **1972**, *136*, 273−281.
(84) Dec, B.; Sobaszek, M.; Jaramillo-Botero, A.; Goddard, W. A.; Bogdanowicz, R. Ligand-Modified Boron-Doped Diamond Surface: DFT Insights into the Electronic Properties of Biofunctionalization. *Materials* **2019**, *12*, 2910.
(85) Stradi, D.; Martinez, U.; Blom, A.; Brandbyge, M.; Stokbro, K. General Atomistic Approach for Modeling Metal-Semiconductor Interfaces Using Density Functional Theory and Nonequilibrium Green's Function. *Phys. Rev. B* **2016**, *93*, 155302.
(86) Xiang, Y.; Jiang, M.; Xiao, H.; Xing, K.; Peng, X.; Zhang, S.; Qi, D.-C. A DFT Study of the Surface Charge Transfer Doping of Diamond by Chromium Trioxide. *Appl. Surf. Sci.* **2019**, *496*, 143604.
(87) Mondal, K.; Ghosh, P. Exfoliation of Ti$_2$C and Ti$_3$C $_2$ Mxenes from Bulk Phases of Titanium Carbide: A Theoretical Prediction. *Solid State Commun.* **2019**, *299*, 113657.
(88) Anasori, B.; Lukatskaya, M. R.; Gogotsi, Y. 2D Metal Carbides and Nitrides (MXenes) for Energy Storage. *Nat. Rev. Mater.* **2017**, *2*, 1−17.
(89) Macak, J. M.; Gong, B. G.; Hueppe, M.; Schmuki, P. Filling of TiO2 Nanotubes by Self-Doping and Electrodeposition. *Adv. Mater.* **2007**, *19*, 3027−3031.
(90) Ryl, J.; Bogdanowicz, R.; Slepski, P.; Sobaszek, M.; Darowicki, K. Dynamic Electrochemical Impedance Spectroscopy (DEIS) as a Tool for Analyzing Surface Oxidation Processes on Boron-Doped Diamond Electrodes. *J. Electrochem. Soc.* **2014**, *161*, H359−H364.
(91) Zha, D.; Xiong, P.; Wang, X. Strongly Coupled Manganese Ferrite/Carbon Black/Polyaniline Hybrid for Low-Cost Supercapacitors with High Rate Capability. *Electrochim. Acta* **2015**, *185*, 218−228.
(92) Lei, C.; Amini, N.; Markoulidis, F.; Wilson, P.; Tennison, S.; Lekakou, C. Activated Carbon from Phenolic Resin with Controlled Mesoporosity for an Electric Double-Layer Capacitor (EDLC). *J. Mater. Chem. A* **2013**, *1*, 6037.
(93) Ryl, J.; Burczyk, L.; Bogdanowicz, R.; Sobaszek, M.; Darowicki, K. Study on Surface Termination of Boron-Doped Diamond Electrodes under Anodic Polarization in H2SO4 by Means of Dynamic Impedance Technique. *Carbon* **2016**, *96*, 1093−1105.
(94) *Supercapacitors: Materials, Systems, and Applications*; Béguin, F., Frąckowiak, E., Eds.; Materials for Sustainable Energy and Development; Wiley-VCH: Weinheim, 2013.
(95) Liu, C.; Yu, Z.; Neff, D.; Zhamu, A.; Jang, B. Z. Graphene-Based Supercapacitor with an Ultrahigh Energy Density. *Nano Lett.* **2010**, *10*, 4863−4868.
(96) Shinde, P. A.; Lokhande, A. C.; Chodankar, N. R.; Patil, A. M.; Kim, J. H.; Lokhande, C. D. Temperature Dependent Surface Morphological Modifications of Hexagonal WO3 Thin Films for High Performance Supercapacitor Application. *Electrochim. Acta* **2017**, *224*, 397−404.
(97) Ramadoss, A.; Kim, S. J. Improved Activity of a Graphene−TiO2 Hybrid Electrode in an Electrochemical Supercapacitor. *Carbon* **2013**, *63*, 434−445.
(98) Gogotsi, Y.; Simon, P. True Performance Metrics in Electrochemical Energy Storage. *Science* **2011**, *334*, 917−918.
(99) Wang, Y.; Song, Y.; Xia, Y. Electrochemical Capacitors: Mechanism, Materials, Systems, Characterization and Applications. *Chem. Soc. Rev.* **2016**, *45*, 5925−5950.
(100) Zhou, J.; Guo, M.; Wang, L.; Ding, Y.; Zhang, Z.; Tang, Y.; Liu, C.; Luo, S. 1T-MoS2 Nanosheets Confined among TiO2 Nanotube Arrays for High Performance Supercapacitor. *Chem. Eng. J.* **2019**, *366*, 163−171.
(101) Pazhamalai, P.; Krishnamoorthy, K.; Mariappan, V. K.; Kim, S.-J. Blue TiO2 Nanosheets as a High-Performance Electrode Material for Supercapacitors. *J. Colloid Interface Sci.* **2019**, *536*, 62−70.

https://dx.doi.org/10.1021/acs.jpcc.0c02792
J. Phys. Chem. C 2020, 124, 15698−15712

(102) Sun, L.; Wang, X.; Wang, Y.; Xiao, D.; Cai, W.; Jing, Y.; Wang, Y.; Hu, F.; Zhang, Q. In-Situ Functionalization of Metal Electrodes for Advanced Asymmetric Supercapacitors. *Front. Chem.* **2019**, *7*, 512.
(103) Chen, T.; Li, M.; Song, S.; Kim, P.; Bae, J. Biotemplate Preparation of Multilayered TiC Nanoflakes for High Performance Symmetric Supercapacitor. *Nano Energy* **2020**, *71*, 104549.
(104) Song, Y.; Xu, J.-L.; Liu, X.-X. Electrochemical Anchoring of Dual Doping Polypyrrole on Graphene Sheets Partially Exfoliated from Graphite Foil for High-Performance Supercapacitor Electrode. *J. Power Sources* **2014**, *249*, 48−58.
(105) Kashani, H.; Chen, L.; Ito, Y.; Han, J.; Hirata, A.; Chen, M. Bicontinuous Nanotubular Graphene−Polypyrrole Hybrid for High Performance Flexible Supercapacitors. *Nano Energy* **2016**, *19*, 391−400.
(106) Zhang, J.; Zhang, Z.; Jiao, Y.; Yang, H.; Li, Y.; Zhang, J.; Gao, P. The Graphene/Lanthanum Oxide Nanocomposites as Electrode Materials of Supercapacitors. *J. Power Sources* **2019**, *419*, 99−105.
(107) Cui, D.; Li, H.; Li, M.; Li, C.; Qian, L.; Zhou, B.; Yang, B. Boron-Doped Graphene Directly Grown on Boron-Doped Diamond for High-Voltage Aqueous Supercapacitors. *ACS Appl. Energy Mater.* **2019**, *2*, 1526−1536.
(108) Cai, Y.; Zhao, B.; Wang, J.; Shao, Z. Non-Aqueous Hybrid Supercapacitors Fabricated with Mesoporous TiO2 Microspheres and Activated Carbon Electrodes with Superior Performance. *J. Power Sources* **2014**, *253*, 80−89.
(109) Wang, G.; Liu, Z. Y.; Wu, J. N.; Lu, Q. Preparation and Electrochemical Capacitance Behavior of TiO2-B Nanotubes for Hybrid Supercapacitor. *Mater. Lett.* **2012**, *71*, 120−122.
(110) Song, Z.; Duan, H.; Zhu, D.; Lv, Y.; Xiong, W.; Cao, T.; Li, L.; Liu, M.; Gan, L. Ternary-Doped Carbon Electrodes for Advanced Aqueous Solid-State Supercapacitors Based on a "Water-in-Salt" Gel Electrolyte. *J. Mater. Chem. A* **2019**, *7*, 15801−15811.
(111) Xue, D.; Zhu, D.; Duan, H.; Wang, Z.; Lv, Y.; Xiong, W.; Li, L.; Liu, M.; Gan, L. Deep-Eutectic-Solvent Synthesis of N/O Self-Doped Hollow Carbon Nanorods for Efficient Energy Storage. *Chem. Commun.* **2019**, *55*, 11219−11222.

https://dx.doi.org/10.1021/acs.jpcc.0c02792
J. Phys. Chem. C 2020, 124, 15698−15712